Title

Infrared plasmons propagate through a hyperbolic nodal metal

Journal

Science Advances, 8(43)

ISSN

2375-2548

Authors

Shao, Yinming
Sternbach, Aaron J
Kim, Brian SY
et al.

Publication Date

2022-10-28

DOI

10.1126/sciadv.add6169

Peer reviewed

PHYSICS

Infrared plasmons propagate through a hyperbolic nodal metal

Yinming Shao[1]*, Aaron J. Sternbach[1], Brian S. Y. Kim[2], Andrey A. Rikhter[3], Xinyi Xu[2], Umberto De Giovannini[4,5], Ran Jing[1], Sang Hoon Chae[2], Zhiyuan Sun[1], Seng Huat Lee[6,7], Yanglin Zhu[6,7], Zhiqiang Mao[6,7], James C. Hone[2], Raquel Queiroz[1], Andrew J. Millis[1,8], P. James Schuck[2], Angel Rubio[4,8], Michael M. Fogler[3], Dmitri N. Basov[1]*

Metals are canonical plasmonic media at infrared and optical wavelengths, allowing one to guide and manipulate light at the nanoscale. A special form of optical waveguiding is afforded by highly anisotropic crystals revealing the opposite signs of the dielectric functions along orthogonal directions. These media are classified as hyperbolic and include crystalline insulators, semiconductors, and artificial metamaterials. Layered anisotropic metals are also anticipated to support hyperbolic waveguiding. However, this behavior remains elusive, primarily because interband losses arrest the propagation of infrared modes. Here, we report on the observation of propagating hyperbolic waves in a prototypical layered nodal-line semimetal ZrSiSe. The observed waveguiding originates from polaritonic hybridization between near-infrared light and nodal-line plasmons. Unique nodal electronic structures simultaneously suppress interband loss and boost the plasmonic response, ultimately enabling the propagation of infrared modes through the bulk of the crystal.

INTRODUCTION

Nodal-line semimetals reveal Dirac-like linear dispersion of electronic bands with nodes extending along lines/loops in the Brillouin zone (Fig. 1A) (*1*, *2*). These systems present an appealing platform to investigate quantum effects originating from the interplay of topology, reduced dimensionality, and electronic correlations encoded in unconventional optical responses (*3*, *4*). Here, we focus on the nodal metal ZrSiSe, which hosts nearly two-dimensional electronic structure and high-mobility Dirac fermions (*2*). We show that the nodal band structure and the attendant van Hove singularities (VHSs) suppress the interband transitions (*5*–*7*) and boost plasmonic response, thus enabling propagation of infrared waveguide modes in metallic samples. We use scanning near-field optical microscopy to visualize the nanoscale infrared signatures of waveguide modes and evaluate their energy-momentum (ω, q) dispersion.

Common materials bounce light at frequencies where the real part of the dielectric function ($\varepsilon = \varepsilon_1 + i\varepsilon_2$) becomes negative. Perhaps counterintuitively, anisotropic media, including layered crystals, do support propagating modes in their interior provided the in-plane and out-of-plane dielectric functions are of opposite sign ($\varepsilon_1^{ab} \cdot \varepsilon_1^{c} < 0$). Because the relevant isofrequency surface (Fig. 1B) is the hyperboloid, these media are referred to as hyperbolic (*8*–*10*). In the hyperbolic regime, the interaction of light with collective modes of crystals yields hyperbolic polaritons imbuing crystals with exotic optical properties, including negative reflection at interfaces (*11*) and ray-like waveguiding in the bulk (*12*, *13*). Hyperbolic waveguiding has mostly been explored in polar insulators inside their narrow phonon bands, including hBN (*14*, *15*), MoO_3 (*16*, *17*), V_2O_5 (*18*), calcite (*19*), Ga_2O_3 (*20*), and semiconducting WSe_2 (*21*). Expanding the spectral bandwidth of hyperbolic polaritons and extending hyperbolicity in the near-infrared frequency range are highly desirable but difficult. Here, we achieved this challenging task by hybridizing light with plasmonic modes of a nodal metal, ZrSiSe.

Hyperbolic waveguiding is anticipated in a wide variety of anisotropic conductors (*8*, *22*–*26*). As the screened plasma frequency ω_p marks the zero crossing of ε_1, a vast frequency range of hyperbolicity appears between $\omega_p^c < \omega < \omega_p^{ab}$, where $\varepsilon_1^{ab} < 0$ and $\varepsilon_1^{c} > 0$ (*27*). While anisotropic metals, in principle, offer broadband hyperbolicity, the inherently strong electronic loss (*28*) prevents waveguiding. It is customary to quantify the electronic loss through the complex optical conductivity ($\sigma = \sigma_1 + i\sigma_2$). The precondition for propagating polaritons $\sigma_2/\sigma_1 \gg 1$ is rarely fulfilled although the hyperbolic plasmons are reported in various electronic systems. Commonly, interband transitions lead to a large σ_1 in the near-infrared range and therefore severely limit the plasmon propagation (*28*). Here, we demonstrate a practical route toward a metal with reduced electronic losses by harnessing the nodal band structure and the attendant VHSs. Our data show that the nodal metal ZrSiSe attains a local minimum of σ_1 near the VHS energy. The sharp reduction in σ_1 that we observe is accompanied by increases in σ_2 that collectively lead to the inequality $\sigma_2/\sigma_1 \gg 1$ over a broad frequency range. The enhanced plasmonic properties along with concurrently reduced interband losses allow for direct experimental observation of propagating hyperbolic plasmon polaritons (HPPs) in the near infrared.

RESULTS

Antenna-launching experiment

To visualize infrared waveguide modes in ZrSiSe, we performed two types of nanoimaging experiments (Fig. 1C). The first one involved placing thin crystals of ZrSiSe on patterned gold antennas, which served as launchers of hyperbolic rays into the interior of the

[1]Department of Physics, Columbia University, New York, NY 10027, USA. [2]Department of Mechanical Engineering, Columbia University, New York, NY 10027, USA. [3]Department of Physics, University of California, San Diego, La Jolla, CA 92093, USA. [4]Max Planck Institute for the Structure and Dynamics of Matter, Center for Free Electron Laser Science, Hamburg 22761, Germany. [5]Università degli Studi di Palermo, Dipartimento di Fisica e Chimica Emilio Segrè, via Archirafi 36, I-90123 Palermo, Italy. [6]Department of Physics, Pennsylvania State University, University Park, PA 16802, USA. [7]2D Crystal Consortium, Materials Research Institute, Pennsylvania State University, University Park, PA 16802, USA. [8]Center for Computational Quantum Physics (CCQ), Flatiron Institute, New York, NY 10010, USA.
*Corresponding author. Email: ys2956@columbia.edu (Y.S.); db3056@columbia.edu (D.N.B.)

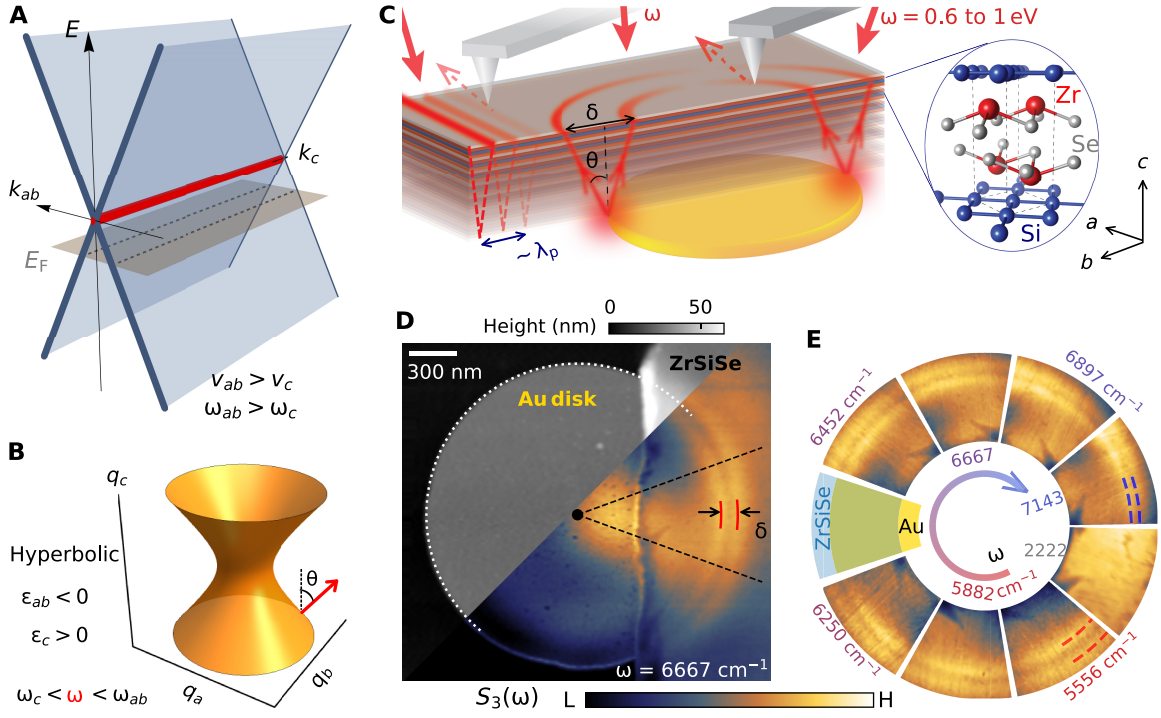

Fig. 1. Infrared waveguide modes in nodal-line metal ZrSiSe. (**A**) Schematic band structure E versus k_{ab}, k_c showing the Dirac nodal line (red). The gray plane indicates the Fermi level. (**B**) Schematic isofrequency surface inside the hyperbolic regime ($\varepsilon_{ab} \cdot \varepsilon_c < 0$) for a nodal-line metal. Red arrow indicates the direction of the group velocity of the hyperbolic ray. (**C**) Schematic of the nanoimaging setup. The near-infrared laser illuminates the sample and hyperbolic plasmon polaritons (HPPs; red lines) are launched by an atomic force microscope (AFM) tip at the edge or by an underlying gold antenna. The AFM-based nano-optics registers the evanescent fields associated with the waveguide modes in the bulk in the form of linear fringes or characteristic rings. The layered crystal structure of ZrSiSe is shown in the inset. (**D**) Topography (gray scale) and near-field scattering amplitude S_3 (color scale) of a 26-nm ZrSiSe crystal partially covering a gold disk. White dotted line indicates the boundary of the Au disk. Red solid lines mark the split center peaks of hyperbolic polariton modes along the circumference. (**E**) Images of S_3 obtained within the sector region indicated by black dashed lines in (D) and assembled for laser frequencies from ω = 7143 to 5556 cm^{-1} within the hyperbolic region. The image taken outside of the hyperbolic range at 2222 cm^{-1} is devoid of the double-ring structure.

sample (*12*, *13*, *21*). The second approach used the sample edge to reflect the HPPs and revealed characteristic higher-order hyperbolic modes (*12*, *15*). The two complementary experiments produced consistent results.

We first focus on experiments involving an Au disk launcher underneath the crystal. As illustrated in Fig. 1C, the HPPs propagate as conical rays and emerge on the top surface of the sample as "hot rings" with enhanced nano-optical contrast surrounding the edge of the Au antennas. The propagation angle θ (with respect to surface normal) is controlled by the anisotropic permittivities of the sample (*12*, *13*, *29*)

$$\tan(\theta) = \sqrt{-\varepsilon_1^{ab}/\varepsilon_1^{c}} = \frac{\delta/2}{d} \quad (1)$$

where δ is the separation of the rings on the top surface and d is the sample thickness. We obtained colocated topography and nano-optical amplitude [$S_3(\omega)$; see Materials and Methods] images of a thin ZrSiSe crystal partially covering the gold disk (Fig. 1D). At ω = 6667 cm^{-1}, a clear double-ring pattern (Fig. 1D) emerges along the Au antenna boundary.

This double-ring pattern is confined to the vicinity of the antenna edges and is distinct from the intensity variation in the interior of our structures prompted by the internal resonances of the Au antenna at much longer length scales. In Fig. 1D, the ring separation (δ≈150 nm) is an order of magnitude smaller than the free-space light wavelength (λ = 1.5 μm, ω ≈ 6667 cm^{-1}). The double-ring pattern also varies with incident light frequency, as shown in Fig. 1E, where we assemble the $S_3(\omega)$ data at selected frequencies. The blue and red dashed lines mark the positions of the hot rings at ω = 7143 and 5556 cm^{-1}, with systematic evolution of the ring separation for frequencies in between. In contrast, the double-ring feature is completely absent in the sector for ω = 2222 cm^{-1} outside of the hyperbolic range quantified in Fig. 2; instead, this sector shows a homogeneous near-field response (see also fig. S6).

We now inquire into quantitative details of propagating HPPs in ZrSiSe. We average the radial line profiles within the sectors depicted in Fig. 1E and plot these in Fig. 2A. The experimental ring separation δ(ω) is obtained by fitting the line profile with two Gaussian functions and a linear background, shown for ω = 7634 and 5556 cm^{-1} in Fig. 2A (see text S3 for complete analysis). With the *ab*-plane permittivity known from (*5*), the experimental ring separation δ, together with the sample thickness d, allows for the extraction of the *c*-axis permittivity of ZrSiSe from Eq. 1. These latter data are displayed in Fig. 2B along with the experimental *ab*-plane permittivity (squares). The hyperbolic regime in ZrSiSe extends between ≈2837 and 9091 cm^{-1} (see texts S1 and S3). Last, we observe yet another hallmark of the hyperbolic rays, which is the scaling of the

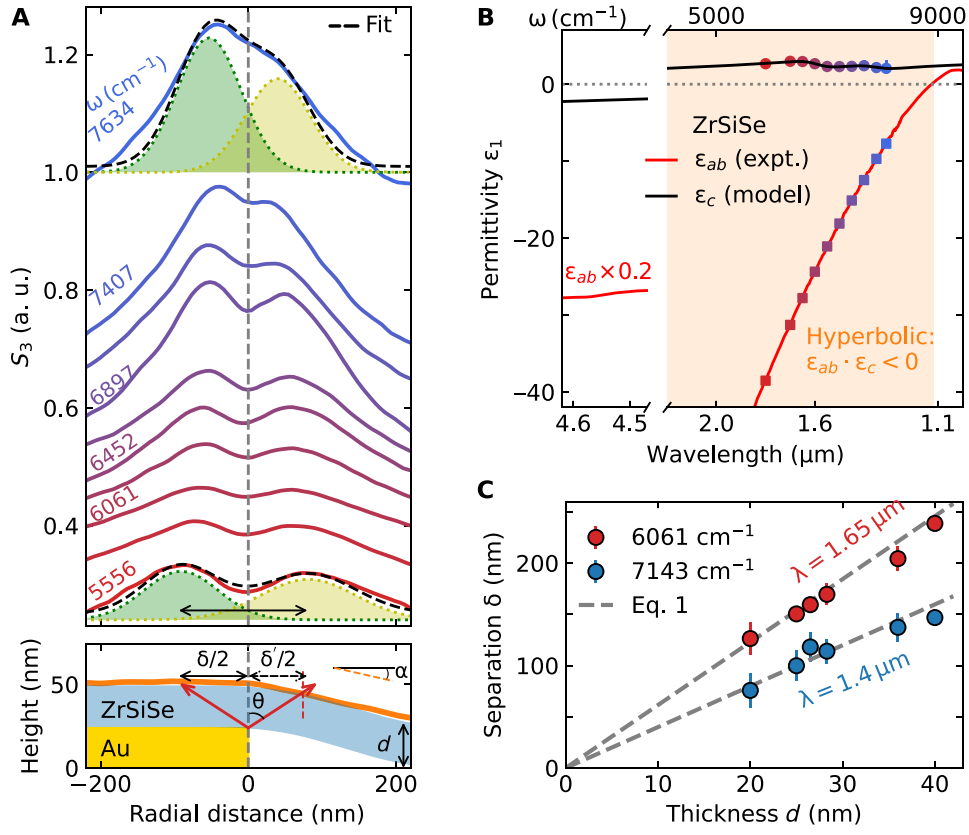

Fig. 2. Hyperbolic electrodynamics of ZrSiSe. (**A**) Line profiles of the near-field scattering amplitude S_3 at several incident frequencies. Black dashed lines are fits using Gaussian functions for the ω = 7634 and 5556 cm^{-1} line profiles. Green and yellow shaded areas indicate the individual Gaussian functions representing the hyperbolic ray profiles. Bottom shows the topography line profile (orange) near the edge of the Au disk (gold) in Fig. 1D. The downward slope (tanα) of the sample (blue) leads to a geometrical correction to the measured ring separation δ. (**B**) In-plane dielectric function (ε_{ab}, red line) obtained from far-field optical measurements (*5*). The ε_{ab} values at selected frequencies (squares) together with δ(ω) in (A) are used to extract ε_c (circles) using Eq. 1. The black line is a Drude-Lorentz fit of the experimental out-of-plane dielectric function data. (**C**) Hyperbolic ray separation δ(ω) as a function of flake thickness *d* at ω = 6061 cm^{-1} (red) and ω = 7143 cm^{-1} (blue). The separations scale linearly with increasing flake thickness, as prescribed by Eq. 1 (gray dashed line).

interpeak separation δ with increasing sample thickness (Fig. 2C), $\delta = 2d\sqrt{-\varepsilon_1^{ab}/\varepsilon_1^{c}}$. Broadband hyperbolic electrodynamics in the layered nodal metal ZrSiSe is therefore firmly established.

Higher-order hyperbolic polariton modes

The natural edges of thin hyperbolic materials can also launch and reflect polaritons emanating from the metallic tip (Fig. 1C) (*30*). To explore HPPs near the edges, we focused on the phase contrast, which provides highest level of image fidelity (*31*–*33*). The phase-contrast data reveal weak higher-order HPP modes: yet another electrodynamics signature of hyperbolicity (*12*, *15*). In Fig. 3 (A to C), we present the topography and near-field phase-contrast images obtained for a 20-nm-thin ZrSiSe crystal on an Si/SiO_2 substrate for two representative laser frequencies. At ω = 8333 cm^{-1} (Fig. 3B), the phase contrast displays a prominent fringe near the edge, which shifts further into the interior of the sample as the laser frequency decreases in Fig. 3C. The first peak-dip separation systematically increases in thicker samples (fig. S15). To quantify the HPP wavelength, we used a previously developed electromagnetic solver (*34*) to simulate the phase contrast with the complex polariton momentum $q_p = (1 + i\gamma)2\pi/\lambda_p$ as input. Here, λ_p is the polariton wavelength, and γ accounts for the damping of the polariton wave.

Multiple fringes of different periodicities appear at lower frequencies and are particularly apparent at ω = 6250 cm^{-1} (Fig. 3C). To better resolve these shorter wavelength oscillations, we inspected the derivative of the phase line profiles, $d\phi_4/dr$. In Fig. 3D, we show the experimental and simulated phase derivative traces for ω= 8333, 6250, and 5000 cm^{-1} (see fig. S13 for additional data). The profile obtained at ω = 8333 cm^{-1} can be adequately reproduced with a single damped polariton of wavelength $\lambda_{p0} \approx 300$ nm. However, for ω = 6250 and 5000 cm^{-1}, an additional mode with a much shorter wavelength λ_{p1} is needed to fully account for the data. Both weaker (q_1) and stronger (q_0) peaks in the derivative line profiles are well described by the simulation (black dashed line) involving two polariton modes with different polaritons of wavelengths λ_{p0} and λ_{p1}. The polariton momentum can then be extracted from the wavelength as $\mathrm{Re}\, q_p = \frac{2\pi}{\lambda p}$, enabling a direct comparison with the theoretical dispersion. As we show below, the two modes correspond to the principal and higher-order HPPs in ZrSiSe and are in accord with the experimental dielectric tensors in Fig. 2B.

The extracted HPP momenta are organized in the dispersion (ω, *q*) plot in Fig. 3E. It is customary to identify HPPs via the divergences of the reflection coefficient $r_p(\omega, q)$ (*14*). A colormap of $\mathrm{Im}(r_p)$ provides an instructive way to visualize both the dispersion

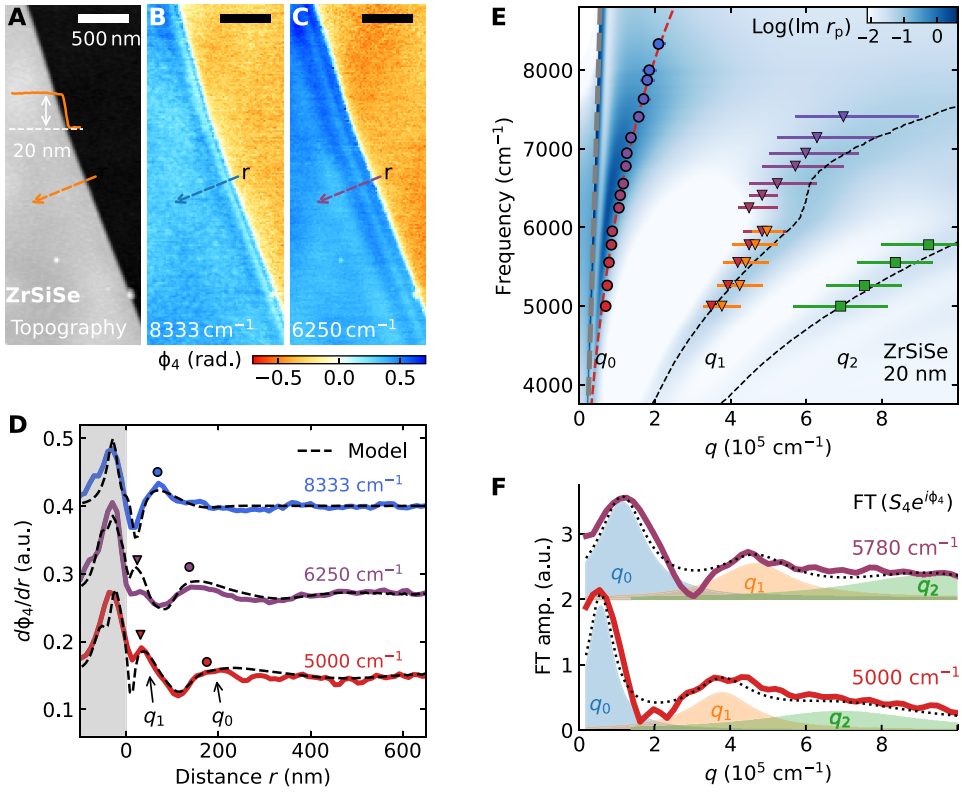

Fig. 3. Hyperbolic plasmon polaritons in ZrSiSe. Topography (**A**) and near-field phase (ϕ_4) image of a 20-nm-thin crystal of ZrSiSe at (**B**) $\omega = 8333\ cm^{-1}$ and (**C**) $\omega = 6250\ cm^{-1}$. (**D**) Phase derivative line profiles ($d\phi_4/dr$) at multiple laser frequencies near edges of ZrSiSe. For $\omega = 6250$ and $5000\ cm^{-1}$, the derivative profiles reveal features at multiple spatial periodicities (q_0 and q_1). Black dashed lines are the simulation of the derivative profile with two periodicities, corresponding to the principal (q_0) and higher-order (q_1) HPPs. a.u., arbitrary units. (**E**) Frequency-momentum dispersion of HPP plotted in the form of Im(r_p). Circles, the principal modes; triangles, higher-order polaritons. Data points are superimposed over the calculated Im(r_p) described in the text. The gray dashed line represents the free-space light cone. Black dashed lines indicate numerical solutions for the divergence of Im(r_p) for the higher-order HPP branches. Red dashed line is a guide for the dispersion of the principal branch. The kink in the experimental dispersion near $\omega \approx 6200\ cm^{-1}$ probably originates from the impact of surface states (fig. S28). (**F**) Fourier transform (FT) of the complex near-field signal $S_4e^{i\phi}{}_4$ along the same path in (B) to (D) at $\omega = 5780$ and $5000\ cm^{-1}$. Multiple peaks in the Fourier transform amplitude correspond to the principal (q_0) and higher-order (q_1, q_2) modes and are fitted by Lorentzian functions (color-shaded area).

and the damping of the HPP modes. The colormap is calculated for a 20-nm-thick crystal of ZrSiSe residing on a SiO_2/Si substrate using experimental dielectric functions (Fig. 2B). As expected, multiple dispersive branches develop in the hyperbolic frequency range, corresponding to the principal and higher-order modes. The existence of higher-order modes can also be documented by directly Fourier transforming the experimental real-space line profile (*12*, *15*). As shown in Fig. 3F, the Fourier transform amplitudes of the complex signal $S_4e^{i\phi}{}_4$ for ω= 5780 and 5000 cm^{-1} (see fig. S14 for additional data) indeed display up to three distinct modes that can be parameterized by Lorentzian functions. The obtained momenta (q_0, q_1) are consistent with the values from line profile modeling (Fig. 3, D and E); Fourier transforms are also suggestive of an additional weaker higher-order mode q_2. The calculated hyperbolic dispersions agree with the experimental momenta (colored circles and triangles), unequivocally corroborating the notion of HPPs in ZrSiSe. The deviation of the higher-order branch (q_1) and the data points (triangles) is within the experimental error bars. Nevertheless, this slight discrepancy hints at the presence of surface states in ZrSiSe (*35*–*37*) with potentially different dielectric responses (see text S4) from the bulk values (Fig. 2B) used in our calculation. Furthermore, around 6200 cm^{-1}, a kink in the experimental dispersion of the q_1 mode shows more pronounced deviation from the prediction based on bulk dielectric constants. This kink structure can also be attributed to the impact of increased metallicity and additional interband transition from the surface state bands (see fig. S28).

DISCUSSION

The propagating HPPs observed in ZrSiSe would not have been possible without tamed interband losses: a unique feat of the nodal band structure uncovered by our experiments. In ZrSiSe, the nodal lines form "squares" in momentum space with lines of VHSs inside the nodal squares (Fig. 4A, inset) (*5*, *7*). The resulting saddle-point structure (Fig. 4A) leads to a suppression of interband transitions above the van Hove energy (Δ). The corresponding dissipative part of the conductivity $\sigma_1(\omega)$ shows a "cliff" above Δ (Fig. 4B), accompanied by a peak in $\sigma_2(\omega)$ at Δ prescribed by Kramers-Kronig relations. We emphasize that the enhancement in $\sigma_2(\omega)$ is an important approach toward high-quality factor plasmons (*28*, *34*, *38*). The unique combination of reduced dissipation (σ_1) and enhanced plasmonic response (σ_2), quantified by the ratio $\frac{\sigma_2}{\sigma_1} \approx$ 3 to 5 for ZrSiSe (Fig. 4C), is superior to that of all other candidate plasmonic and excitonic hyperbolic materials reported so far. The plasmonic

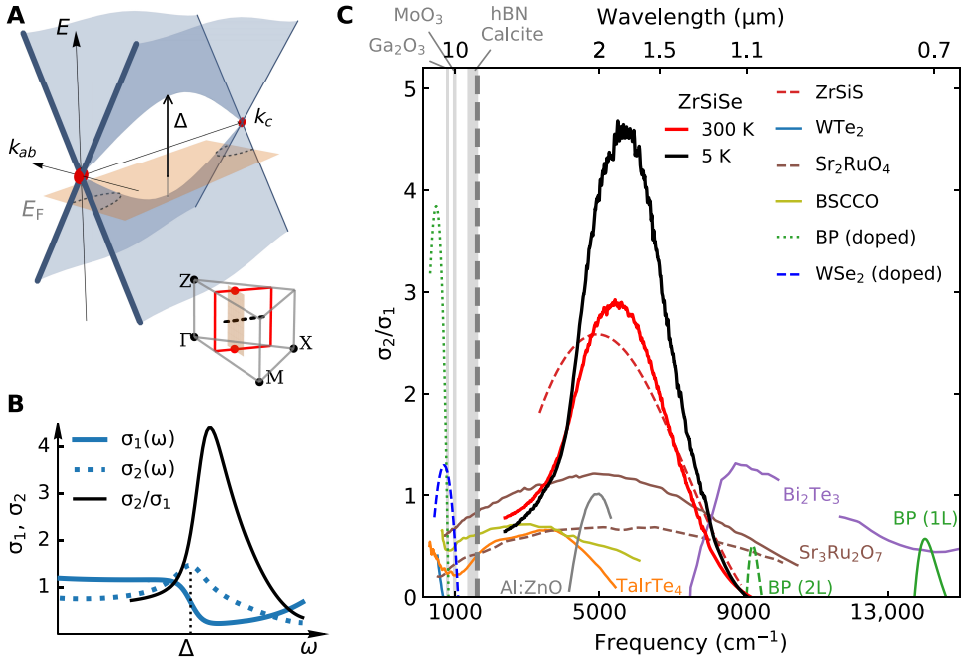

Fig. 4. Band structure origin of enhanced plasmonic hyperbolicity in a nodal metal. (**A**) Schematic band structure E versus k_{ab}, k_c inside the nodal square (red line in inset). Vertical arrow indicates the van Hove energy Δ. (**B**) Model for the interband optical conductivity ($\sigma = \sigma_1 + i\sigma_2$) of a nodal line near the van Hove energy (see Materials and Methods). The ratio σ_2/σ_1 exhibits a maximum near Δ. The optical conductivity is related to the dielectric function via $\sigma = i\omega(1-\varepsilon)/4\pi$. (**C**) Survey of experimental σ_2/σ_1 ratio for representative plasmonic hyperbolic materials [WTe_2 (*22*, *23*), $TaIrTe_4$ (*24*), ZrSiS (*25*), black phosphorus (BP) (*26*), doped WSe_2 (*21*), $Bi_2Sr_2CaCu_2O_8$ (*42*, *43*), Sr_2RuO_4 (*44*), $Sr_3Ru_2O_7$ (*45*), and Bi_2Te_3 (*46*)], metamaterial Al:ZnO (*47*), and excitonic hyperbolic materials [few-layer BP (*48*)]. (See figs. S20 to S27 for extracted optical conductivities).

qualities in ZrSiSe are anticipated to be further enhanced at cryogenic temperatures (Fig. 4C, black curve).

The suppression of interband transitions near the van Hove energy offers a novel strategy for the "band structure engineering" approach to mitigating loss and boosting plasmonic response (*39*, *40*). While the existence of "loss-less metal" remains elusive (*28*), we propose that VHSs in topological systems (*41*) reveal as-yet untapped plasmonic design rule afforded by nodal-line semimetals.

MATERIALS AND METHODS

Single crystal growth and device fabrication

The ZrSiSe single crystals were synthesized using a chemical vapor transport method as described previously (*2*, *5*). For Au antenna–patterned devices, Au/Cr (25 nm/1 nm) disks were e-beam–deposited on SiO_2/Si substrates following standard e-beam lithography processes using a lift-off resist. ZrSiSe flakes were then directly exfoliated on Au/Cr disks in a glove box filled with inert gas [O_2 < 1 part per million (ppm), H_2O < 0.1 ppm]. Before exfoliation, the substrates were annealed in glove box at 250°C for 1 hour to remove any residual moisture on the surface.

Near-infrared nano-optical measurements

We used a scattering-type scanning near-field optical microscope (Neaspec) based on an atomic force microscope (AFM) operating in tapping mode. The tapping frequency of the AFM tip is around 70 kHz, and near-field data are collected at higher harmonic (n = 3 or 4) of the tapping frequency to suppress the far-field background. For the gold antenna launcher experiment, the difference frequency generation outputs of a pulsed laser source (Pharos, Light Conversion) were used. We used a continuous-wave tunable laser from M Squared to obtain phase contrast images near the edges of thin crystals. Tunable outputs between 1140 and 2200 nm are generated by frequency mixing of a high-power 532-nm diode laser (Equinox) and a Ti:sapphire laser tunable between 700 and 1000 nm (SolsTiS).

Geometrical correction considering finite antenna thickness

Because of the finite thickness of the underlying Au antenna, the sample exhibits a downward slope outside the antenna boundary (Fig. 2A, bottom). This small slope (tanα) leads to a finite asymmetry ($\frac{\delta}{2} > \frac{\delta'}{2}$) in the propagation distance of the two rays (Fig. 2A), which we corrected in the extraction of δ(ω) as following. The two distances δ and δ′ are related by $\frac{\delta}{\delta'} = 1 + \tan\alpha \cdot \tan\theta$, where $\tan\theta = \frac{\delta}{2d}$ and d is the sample thickness. The measured double-ring distance is denoted as $\Delta = \frac{\delta}{2} + \frac{\delta'}{2}$. Substituting δ′ in terms of Δ and δ, we obtained $\delta = \Delta - \frac{2d}{\tan\alpha} + \sqrt{\Delta^2 + \frac{4d^2}{\tan^2\alpha}}$. At the limit of $\alpha \to 0$ (no downward slope) or $d \to \infty$ (infinitely thick sample), $\sqrt{\Delta^2 + \frac{4d^2}{\tan^2\alpha}} \approx \frac{2d}{\tan\alpha}$ and therefore, $\delta \to \Delta$ as expected.

Model for interband optical conductivity of ZrSiSe near VHS

The minimum in the interband optical conductivity of ZrSiSe (see fig. S1) can be modeled by a step function near the VHSs and a Lorentzian function accounting for transitions at higher energy. Specifically, the step function is expressed as $\sigma_{step}(\omega) = \frac{\tanh[(-\omega+\Delta)/\Gamma]+1}{2} + \sigma_s$, where Δ is the van Hove energy, Γ is the step width, and σ_s is a constant

background. The higher-energy optical transition is described by $\sigma_{high}(\omega) = -i\omega[\varepsilon_\infty - 1 + f^2/({\omega_0}^2 - \omega^2 - i\gamma\omega)]$, where ε_∞ is the high-frequency dielectric constant; f^2, ω_0, and γ are the oscillator strength, center frequency, and scattering rate of the Lorentzian peak, respectively. The real part of the interband optical conductivity of ZrSiSe can then be expressed as $\sigma_1 = \sigma_{step}(\omega) + \mathrm{Re}\,[\sigma_{high}(\omega)]$, and the imaginary part σ_2 are obtained numerically through Kramers-Kronig relations. For modeled σ_1 and σ_2 shown in Fig. 4B, the following parameters are used: $\Delta = 1.25$, $\Gamma = 0.06$, $\sigma_s = 0.1$, $\omega_0 = 2$, $f^2 = 0.49$, $\gamma = 0.5$, and $\varepsilon_\infty = 2.5$.

SUPPLEMENTARY MATERIALS

Supplementary material for this article is available at https://science.org/doi/10.1126/sciadv.add6169

REFERENCES AND NOTES

1. L. M. Schoop, M. N. Ali, C. Straßer, A. Topp, A. Varykhalov, D. Marchenko, V. Duppel, S. S. P. Parkin, B. V. Lotsch, C. R. Ast, Dirac cone protected by non-symmorphic symmetry and three-dimensional Dirac line node in ZrSiS. *Nat. Commun.* **7**, 11696 (2016).
2. J. Hu, Z. Tang, J. Liu, X. Liu, Y. Zhu, D. Graf, K. Myhro, S. Tran, C. N. Lau, J. Wei, Z. Mao, Evidence of topological nodal-line fermions in ZrSiSe and ZrSiTe. *Phys. Rev. Lett.* **117**, 016602 (2016).
3. N. P. Armitage, E. J. Mele, A. Vishwanath, Weyl and Dirac semimetals in three-dimensional solids. *Rev. Mod. Phys.* **90**, 015001 (2018).
4. J. Orenstein, J. E. Moore, T. Morimoto, D. H. Torchinsky, J. W. Harter, D. Hsieh, Topology and symmetry of quantum materials via nonlinear optical responses. *Annu. Rev. Condens. Matter Phys.* **12**, 247–272 (2021).
5. Y. Shao, A. N. Rudenko, J. Hu, Z. Sun, Y. Zhu, S. Moon, A. J. Millis, S. Yuan, A. I. Lichtenstein, D. Smirnov, Z. Q. Mao, M. I. Katsnelson, D. N. Basov, Electronic correlations in nodal-line semimetals. *Nat. Phys.* **16**, 636–641 (2020).
6. M. B. Schilling, L. M. Schoop, B. V. Lotsch, M. Dressel, A. V. Pronin, Flat optical conductivity in ZrSiS due to two-dimensional Dirac bands. *Phys. Rev. Lett.* **119**, 187401 (2017).
7. T. Habe, M. Koshino, Dynamical conductivity in the topological nodal-line semimetal ZrSiS. *Phys. Rev. B.* **98**, 125201 (2018).
8. E. E. Narimanov, A. V. Kildishev, Naturally hyperbolic. *Nat. Photon.* **9**, 214–216 (2015).
9. H. N. S. Krishnamoorthy, Z. Jacob, E. Narimanov, I. Kretzschmar, V. M. Menon, Topological transitions in metamaterials. *Science* **336**, 205–209 (2012).
10. A. V. Kildishev, A. Boltasseva, V. M. Shalaev, Planar photonics with metasurfaces. *Science* **339**, 1232009 (2013).
11. G. Álvarez-Pérez, J. Duan, J. Taboada-Gutiérrez, Q. Ou, E. Nikulina, S. Liu, J. H. Edgar, Q. Bao, V. Giannini, R. Hillenbrand, J. Martín-Sánchez, A. Y. Nikitin, P. Alonso-González, Negative reflection of nanoscale-confined polaritons in a low-loss natural medium. *Sci. Adv.* **8**, eabp8486 (2022).
12. S. Dai, Q. Ma, T. Andersen, A. S. Mcleod, Z. Fei, M. K. Liu, M. Wagner, K. Watanabe, T. Taniguchi, M. Thiemens, F. Keilmann, P. Jarillo-Herrero, M. M. Fogler, D. N. Basov, Subdiffractional focusing and guiding of polaritonic rays in a natural hyperbolic material. *Nat. Commun.* **6**, 6963 (2015).
13. P. Li, M. Lewin, A. V. Kretinin, J. D. Caldwell, K. S. Novoselov, T. Taniguchi, K. Watanabe, F. Gaussmann, T. Taubner, Hyperbolic phonon-polaritons in boron nitride for near-field optical imaging and focusing. *Nat. Commun.* **6**, 7507 (2015).
14. S. Dai, Z. Fei, Q. Ma, A. S. Rodin, M. Wagner, A. S. McLeod, M. K. Liu, W. Gannett, W. Regan, K. Watanabe, T. Taniguchi, M. Thiemens, G. Dominguez, A. H. C. Neto, A. Zettl, F. Keilmann, P. Jarillo-Herrero, M. M. Fogler, D. N. Basov, Tunable phonon polaritons in atomically thin van der Waals crystals of boron nitride. *Science* **343**, 1125–1129 (2014).
15. A. J. Giles, S. Dai, I. Vurgaftman, T. Hoffman, S. Liu, L. Lindsay, C. T. Ellis, N. Assefa, I. Chatzakis, T. L. Reinecke, J. G. Tischler, M. M. Fogler, J. H. Edgar, D. N. Basov, J. D. Caldwell, Ultralow-loss polaritons in isotopically pure boron nitride. *Nat. Mater.* **17**, 134–139 (2018).
16. W. Ma, P. Alonso-González, S. Li, A. Y. Nikitin, J. Yuan, J. Martín-Sánchez, J. Taboada-Gutiérrez, I. Amenabar, P. Li, S. Vélez, C. Tollan, Z. Dai, Y. Zhang, S. Sriram, K. Kalantar-Zadeh, S.-T. Lee, R. Hillenbrand, Q. Bao, In-plane anisotropic and ultra-low-loss polaritons in a natural van der Waals crystal. *Nature* **562**, 557–562 (2018).
17. Z. Zheng, N. Xu, S. L. Oscurato, M. Tamagnone, F. Sun, Y. Jiang, Y. Ke, J. Chen, W. Huang, W. L. Wilson, A. Ambrosio, S. Deng, H. Chen, A mid-infrared biaxial hyperbolic van der Waals crystal. *Sci. Adv.* **5**, eaav8690 (2019).
18. J. Taboada-Gutiérrez, G. Álvarez-Pérez, J. Duan, W. Ma, K. Crowley, I. Prieto, A. Bylinkin, M. Autore, H. Volkova, K. Kimura, T. Kimura, M.-H. Berger, S. Li, Q. Bao, X. P. A. Gao, I. Errea, A. Y. Nikitin, R. Hillenbrand, J. Martín-Sánchez, P. Alonso-González, Broad spectral tuning of ultra-low-loss polaritons in a van der Waals crystal by intercalation. *Nat. Mater.* **19**, 964–968 (2020).
19. W. Ma, G. Hu, D. Hu, R. Chen, T. Sun, X. Zhang, Q. Dai, Y. Zeng, A. Alù, C.-W. Qiu, P. Li, Ghost hyperbolic surface polaritons in bulk anisotropic crystals. *Nature* **596**, 362–366 (2021).
20. N. C. Passler, X. Ni, G. Hu, J. R. Matson, G. Carini, M. Wolf, M. Schubert, A. Alù, J. D. Caldwell, T. G. Folland, A. Paarmann, Hyperbolic shear polaritons in low-symmetry crystals. *Nature* **602**, 595–600 (2022).
21. A. J. Sternbach, S. H. Chae, S. Latini, A. A. Rikhter, Y. Shao, B. Li, D. Rhodes, B. Kim, P. J. Schuck, X. Xu, X.-Y. Zhu, R. D. Averitt, J. Hone, M. M. Fogler, A. Rubio, D. N. Basov, Programmable hyperbolic polaritons in van der Waals semiconductors. *Science* **371**, 617–620 (2021).
22. A. J. Frenzel, C. C. Homes, Q. D. Gibson, Y. M. Shao, K. W. Post, A. Charnukha, R. J. Cava, D. N. Basov, Anisotropic electrodynamics of type-II Weyl semimetal candidate WTe2. *Phys. Rev. B.* **95**, 245140 (2017).
23. C. Wang, S. Huang, Q. Xing, Y. Xie, C. Song, F. Wang, H. Yan, Van der Waals thin films of WTe_2 for natural hyperbolic plasmonic surfaces. *Nat. Comm.* **11**, 1158 (2020).
24. Y. Shao, R. Jing, S. H. Chae, C. Wang, Z. Sun, E. Emmanouilidou, S. Xu, D. Halbertal, B. Li, A. Rajendran, F. L. Ruta, L. Xiong, Y. Dong, A. S. McLeod, S. S. Sunku, J. C. Hone, J. Moore, J. Orenstein, J. G. Analytis, A. J. Millis, N. Ni, D. Xiao, D. N. Basov, Nonlinear nanoelectrodynamics of a Weyl metal. *Proc. Natl. Acad. Sci. U.S.A.* **118**, e2116366118 (2021).
25. J. Ebad-Allah, S. Rojewski, M. Vöst, G. Eickerling, W. Scherer, E. Uykur, R. Sankar, L. Varrassi, C. Franchini, K.-H. Ahn, J. Kuneš, C. A. Kuntscher, Pressure-induced excitations in the out-of-plane optical response of the nodal-line semimetal ZrSiS. *Phys. Rev. Lett.* **127**, 076402 (2021).
26. S. Biswas, W. S. Whitney, M. Y. Grajower, K. Watanabe, T. Taniguchi, H. A. Bechtel, G. R. Rossman, H. A. Atwater, Tunable intraband optical conductivity and polarization-dependent epsilon-near-zero behavior in black phosphorus. *Sci. Adv.* **7**, eabd4623 (2021).
27. T. Low, A. Chaves, J. D. Caldwell, A. Kumar, N. X. Fang, P. Avouris, T. F. Heinz, F. Guinea, L. Martin-Moreno, F. Koppens, Polaritons in layered two-dimensional materials. *Nat. Mater.* **16**, 182–194 (2017).
28. A. Boltasseva, H. A. Atwater, Low-loss plasmonic metamaterials. *Science* **331**, 290–291 (2011).
29. J. D. Caldwell, A. V. Kretinin, Y. Chen, V. Giannini, M. M. Fogler, Y. Francescato, C. T. Ellis, J. G. Tischler, C. R. Woods, A. J. Giles, M. Hong, K. Watanabe, T. Taniguchi, S. A. Maier, K. S. Novoselov, Sub-diffractional volume-confined polaritons in the natural hyperbolic material hexagonal boron nitride. *Nat. Commun.* **5**, 5221 (2014).
30. S. Dai, Q. Ma, Y. Yang, J. Rosenfeld, M. D. Goldflam, A. McLeod, Z. Sun, T. I. Andersen, Z. Fei, M. Liu, Y. Shao, K. Watanabe, T. Taniguchi, M. Thiemens, F. Keilmann, P. Jarillo-Herrero, M. M. Fogler, D. N. Basov, Efficiency of launching highly confined polaritons by infrared light incident on a hyperbolic material. *Nano Lett.* **17**, 5285–5290 (2017).
31. J. A. Gerber, S. Berweger, B. T. O'Callahan, M. B. Raschke, Phase-resolved surface plasmon interferometry of graphene. *Phys. Rev. Lett.* **113**, 055502 (2014).
32. Z. Shi, H. A. Bechtel, S. Berweger, Y. Sun, B. Zeng, C. Jin, H. Chang, M. C. Martin, M. B. Raschke, F. Wang, Amplitude- and phase-resolved nanospectral imaging of phonon polaritons in hexagonal boron nitride. *ACS Photonics* **2**, 790–796 (2015).
33. S. Dai, W. Fang, N. Rivera, Y. Stehle, B.-Y. Jiang, J. Shen, R. Y. Tay, C. J. Ciccarino, Q. Ma, D. Rodan-Legrain, P. Jarillo-Herrero, E. H. T. Teo, M. M. Fogler, P. Narang, J. Kong, D. N. Basov, Phonon polaritons in monolayers of hexagonal boron nitride. *Adv. Mater.* **31**, 1806603 (2019).
34. Z. Fei, A. S. Rodin, G. O. Andreev, W. Bao, A. S. McLeod, M. Wagner, L. M. Zhang, Z. Zhao, M. Thiemens, G. Dominguez, M. M. Fogler, A. H. C. Neto, C. N. Lau, F. Keilmann, D. N. Basov, Gate-tuning of graphene plasmons revealed by infrared nano-imaging. *Nature* **487**, 82–85 (2012).
35. Z. Zhu, T.-R. Chang, C.-Y. Huang, H. Pan, X.-A. Nie, X.-Z. Wang, Z.-T. Jin, S.-Y. Xu, S.-M. Huang, D.-D. Guan, S. Wang, Y.-Y. Li, C. Liu, D. Qian, W. Ku, F. Song, H. Lin, H. Zheng, J.-F. Jia, Quasiparticle interference and nonsymmorphic effect on a floating band surface state of ZrSiSe. *Nat. Commun.* **9**, 4153 (2018).
36. S. Xue, M. Wang, Y. Li, S. Zhang, X. Jia, J. Zhou, Y. Shi, X. Zhu, Y. Yao, J. Guo, Observation of nodal-line plasmons in ZrSiS. *Phys. Rev. Lett.* **127**, 186802 (2021).
37. A. Topp, R. Queiroz, A. Grüneis, L. Müchler, A. W. Rost, A. Varykhalov, D. Marchenko, M. Krivenkov, F. Rodolakis, J. L. McChesney, B. V. Lotsch, L. M. Schoop, C. R. Ast, Surface floating 2D bands in layered nonsymmorphic semimetals: ZrSiS and related compounds. *Phys. Rev. X.* **7**, 041073 (2017).
38. J. Chen, M. Badioli, P. Alonso-González, S. Thongrattanasiri, F. Huth, J. Osmond, M. Spasenović, A. Centeno, A. Pesquera, P. Godignon, A. Zurutuza Elorza, N. Camara, F. J. G. de Abajo, R. Hillenbrand, F. H. L. Koppens, Optical nano-imaging of gate-tunable graphene plasmons. *Nature* **487**, 77–81 (2012).
39. M. N. Gjerding, M. Pandey, K. S. Thygesen, Band structure engineered layered metals for low-loss plasmonics. *Nat. Commun.* **8**, 15133 (2017).
40. C. Lewandowski, L. Levitov, Intrinsically undamped plasmon modes in narrow electron bands. *Proc. Natl. Acad. Sci. U.S.A.* **116**, 20869–20874 (2019).

41. N. F. Q. Yuan, H. Isobe, L. Fu, Magic of high-order van Hove singularity. *Nat. Commun.* **10**, 5769 (2019).
42. S. Tajima, G. D. Gu, S. Miyamoto, A. Odagawa, N. Koshizuka, Optical evidence for strong anisotropy in the normal and superconducting states in $Bi_2Sr_2CaCu_2O_{8+z}$. *Phys. Rev. B.* **48**, 16164–16167 (1993).
43. M. E. Berkowitz, B. S. Y. Kim, G. Ni, A. S. McLeod, C. F. B. Lo, Z. Sun, G. Gu, K. Watanabe, T. Taniguchi, A. J. Millis, J. C. Hone, M. M. Fogler, R. D. Averitt, D. N. Basov, Hyperbolic cooper-pair polaritons in planar graphene/cuprate plasmonic cavities. *Nano Lett.* **21**, 308–316 (2021).
44. T. Katsufuji, M. Kasai, Y. Tokura, In-plane and out-of-plane optical spectra of Sr_2RuO_4. *Phys. Rev. Lett.* **76**, 126–129 (1996).
45. C. Mirri, L. Baldassarre, S. Lupi, M. Ortolani, R. Fittipaldi, A. Vecchione, P. Calvani, Anisotropic optical conductivity of $Sr_3Ru_2O_7$. *Phys. Rev. B.* **78**, 155132 (2008).
46. M. Esslinger, R. Vogelgesang, N. Talebi, W. Khunsin, P. Gehring, S. de Zuani, B. Gompf, K. Kern, Tetradymites as natural hyperbolic materials for the near-infrared to visible. *ACS Photonics* **1**, 1285–1289 (2014).
47. G. V. Naik, J. Liu, A. V. Kildishev, V. M. Shalaev, A. Boltasseva, Demonstration of Al:ZnO as a plasmonic component for near-infrared metamaterials. *Proc. Natl. Acad. Sci. U.S.A.* **109**, 8834–8838 (2012).
48. F. Wang, C. Wang, A. Chaves, C. Song, G. Zhang, S. Huang, Y. Lei, Q. Xing, L. Mu, Y. Xie, H. Yan, Prediction of hyperbolic exciton-polaritons in monolayer black phosphorus. *Nat. Comm.* **12**, 5628 (2021).
49. B. Xu, Y. M. Dai, L. X. Zhao, K. Wang, R. Yang, W. Zhang, J. Y. Liu, H. Xiao, G. F. Chen, A. J. Taylor, D. A. Yarotski, R. P. Prasankumar, X. G. Qiu, Optical spectroscopy of the Weyl semimetal TaAs. *Phys. Rev. B.* **93**, 121110 (2016).
50. C. J. Tabert, J. P. Carbotte, Optical conductivity of Weyl semimetals and signatures of the gapped semimetal phase transition. *Phys. Rev. B.* **93**, 085442 (2016).
51. A. Sommerfeld, O. Laporte, P. A. Moldauer, Optics: Vol. 5 of lectures on theoretical physics. *Phys. Today* **8**, 16 (1955).
52. P. C. Clemmow, A method for the exact solution of a class of two-dimensional diffraction problems. *Proc. R. Soc. Lond. A.* **205**, 286–308 (1951).
53. N. Tancogne-Dejean, A. Rubio, Parameter-free hybridlike functional based on an extended Hubbard model: DFT+*U*+*V*. *Phys. Rev. B.* **102**, 155117 (2020).
54. N. Tancogne-Dejean, M. J. T. Oliveira, X. Andrade, H. Appel, C. H. Borca, G. le Breton, F. Buchholz, A. Castro, S. Corni, A. A. Correa, U. de Giovannini, A. Delgado, F. G. Eich, J. Flick, G. Gil, A. Gomez, N. Helbig, H. Hübener, R. Jestädt, J. Jornet-Somoza, A. H. Larsen, I. V. Lebedeva, M. Lüders, M. A. L. Marques, S. T. Ohlmann, S. Pipolo, M. Rampp, C. A. Rozzi, D. A. Strubbe, S. A. Sato, C. Schäfer, I. Theophilou, A. Welden, A. Rubio, Octopus, a computational framework for exploring light-driven phenomena and quantum dynamics in extended and finite systems. *J. Chem. Phys.* **152**, 124119 (2020).
55. G. Gatti, A. Crepaldi, M. Puppin, N. Tancogne-Dejean, L. Xian, U. De Giovannini, S. Roth, S. Polishchuk, P. Bugnon, A. Magrez, H. Berger, F. Frassetto, L. Poletto, L. Moreschini, S. Moser, A. Bostwick, E. Rotenberg, A. Rubio, M. Chergui, M. Grioni, Light-induced renormalization of the Dirac quasiparticles in the nodal-line semimetal ZrSiSe. *Phys. Rev. Lett.* **125**, 076401 (2020).
56. C. Hartwigsen, S. Goedecker, J. Hutter, Relativistic separable dual-space Gaussian pseudopotentials from H to Rn. *Phys. Rev. B.* **58**, 3641–3662 (1998).

Acknowledgments

Funding: Research in the physics of Dirac electrons at Columbia is supported by DOE-BES grant DE-SC0018426. The research in nano-light imaging methods is supported through the Vannevar Bush Faculty Fellow ONR-VB: N00014-19-1-2630. The development of nano-imaging capabilities in near-infrared is funded by the Vannevar Bush Faculty Fellowship ONR-VB: N00014-19-1-2630. D.N.B. is a Moore Investigator in Quantum Materials EPIQS GBMF9455. Nonlinear imaging and spectroscopy are funded supported as part of Programmable Quantum Materials, an Energy Frontier Research Center funded by the U.S. Department of Energy (DOE), Office of Science, Basic Energy Sciences (BES), under award DE-SC0019443. The financial support for sample preparation and characterization was provided by the National Science Foundation through the Penn State 2D Crystal Consortium-Materials Innovation Platform (2DCC-MIP) under NSF cooperative agreement DMR-1539916 and DMR-2039351. U.D.G. and A.R. acknowledge support from the European Research Council (ERC-2015-AdG-694097), Grupos Consolidados (IT1249-19), and SFB925. We acknowledge funding by the Deutsche Forschungsgemeinschaft (DFG, German Research Foundation) under Germany's Excellence Strategy - Cluster of Excellence and Advanced Imaging of Matter (AIM) EXC 2056 - 390715994 and RTG 2247. This work was supported by the Max Planck-New York City Center for Nonequilibrium Quantum Phenomena. The Flatiron Institute is a division of the Simons Foundation. **Author contributions:** Y.S. and D.N.B. conceived the study. Y.S. and A.J.S. performed the near-field experiments. B.S.Y.K. fabricated the device with assistance from S.H.C. and supervised by J.C.H. A.A.R. performed the electrodynamic simulation with supervision from M.M.F. Y.Z. and S.H.L. grew the single crystals and performed transport measurements supervised by Z.M. U.D.G. performed first principal calculations with supervision from A.R. Y.S. and D.N.B. wrote the manuscript with input from all coauthors. **Competing interests:** The authors declare that they have no competing interests. **Data and materials availability:** All data needed to evaluate the conclusions in the paper are present in the paper and/or the Supplementary Materials.

Submitted 22 June 2022
Accepted 8 September 2022
Published 26 October 2022
10.1126/sciadv.add6169